Indian Journal of Engineering & Materials Sciences
Vol. 27, February 2020, pp. 5-18

Vacuum Oxy-nitro carburizing of tool steels: structure and mechanical reliability

Maria Nikolova[a], Danail Nikolov[a], Emil Yankov[a], Bora Derin[b] & Slavcho Topalski[c]

[a]Deptartment of Material Science and Technology, University of Ruse A. Kanchev, 8 Studentska Str., 7017 Ruse, Bulgaria
[b]Metallurgical and Materials Engineering Department, Istanbul Technical University, 34469 Maslak, Istanbul, Turkey
[c]Fraunhofer Institute for Material and Beam Technology, IWS, Dortmunder Oberflächen Centrum DOC, 44145 Dortmund, Germany

Received: 23 April 2018; Accepted: 06 December 2019

AISI H10, H11, H21, and D2 have been vacuum oxy-nitrocarburizing at 570 °C in cycling gas flow manner. Metastable diagram calculations belonging to Fe-N-C and Fe-N-C-X systems (X = Cr, Mo, W), have been performed by using "phase diagram" module of FactSageto predict the steels' phase compositions. The reactive diffusion of both N and C into the tempered martensite has been discussed on the base of different chemical composition, size, and distribution of phases in the microstructure. The compound layers consisted mainly of not pre-saturated and poreless ε-carbonitride and magnetite (Fe_3O_4). In D2 steel, nitrogen diffusion caused a complete transformation of the primary carbides in 50 μm depths from the surface affecting the growth of grain boundary carbides. In contrast to the sharp compound/diffusion layer interface of H10, H11, and D2 steels, in H21 carbon and nitrogen were deeply absorbed in the diffusion layer while chromium strongly increased underneath the surface. The vacuum process enhanced the hardness and decreased the friction coefficients down to 0.13-0.15 at 100 N normal load for all samples. Since the compound layer thickness was relatively small for all tool steels, the phase composition and structure of the diffusion layers were found to be crucial for the scratch wear performance.

Keywords: Thermochemical modeling, SEM, Phase composition, GDOES, Microhardness, Scratch test

1 Introduction

Tool steels are widely used in machinery industries for the manufacturing of components in medium-large series production. The wear resistance of dies, cutting tools and plastic molds for hot and cold working depends on the combination of high surface hardness with a low coefficient of friction and sufficiently tough steel core. To obtain the necessary tribomechanical properties a suitable thermo-chemical treatment should be applied thereby modifying the surface microstructure, hardness, and toughness of the engineering components that are subject to sliding, rolling or cutting friction. The fast degradation of the working surfaces could lead to extensive economic losses.

For better mechanical and tribological properties, different surface thermochemical treatments or coating procedures that reduce the coefficient of friction and increase the durability of the material are being used. An effective way to enhance the tribological properties and harden the surface of the quenched-tempered tools used in the forming industry is by applying ferritic thermochemical treatments like nitriding and nitro-carburizing. The low treatment temperatures (< 591°C) enhance the surface properties of the machine part without changing its shape and dimensions or compromising the core strength. In contrast to nitriding, the nitrocarburizing processes indicate many advantages like effectiveness, shorter treatment time, harder and tougher compound layer with higher wear resistance. The nitrogen and carbon atoms basically react with the iron and alloying elements forming surface compound and underlying diffusion layers. Riofano *et al.*[1] found out that the wear of both layers depends on the nitrogen content in the surface and matrix and the number and distribution of the precipitates in them. The oxidation could be applied before (pre-oxidation), after (post-oxidation) and simultaneously (oxy-nitrocarburizing (ONC)) and in the latter case, the addition of oxidation agents during the nitrocarburizing accelerates the process and improves the surface properties[2].

The wear behavior of the compound layer depends on its composition, thickness, and porosity. The heterophase structure of the compound layer generates internal stresses that could affect the surface performance in different wear conditions. The presence of monolayered

*Corresponding author (E-mail: mpnikolova@uni-ruse.bg)

ε-Fe_{2-3}(N,C) is considered as tribologically desirable because of its higher hardness, toughness and anti-scuffing properties, while γ`-phase is claimed to be brittle[3]. The thick compound layer with a porous structure that is usually obtained after the conventional gas nitro-carburizing process is brittle and its fast-breaking down could reduce the tool life. Therefore, the small thickness of the surface nitride layer could enable good ductility of the hard surface and small dimensional changes of the machine parts. Our research group[4,5] discovered that during the vacuum oxy-nitrocarburizing (ONC) process the saturation conditions could be established in a way that minimizes the compound layer thickness, increases surface hardness, and therefore, improves wear resistance. The surface compound and underlying diffusion layers are formed *via* thermo-chemical treatment in NH_3 and CO_2 containing atmospheres. The low pressure during the initial hours of saturation increases the nitrogen potential of the atmosphere and simultaneously, the cycling pumping of exhausted gases clears the chemisorbed gas products from the surface at regular intervals. The vacuum ONC process offers the ability to carry out simple and reliable thermochemical treatment that is characterized by high efficiency, the ability of properties control and environmental-friendly aspects. The main advantage of the vacuum ONC process is the lower gas consumption – the amount of NH_3 and CO_2 is equal to 0.32 m^3/h and 0.08 m^3/h, respectively together with overall 0.34 m^3 N_2 exhausted for a 7-hour process. For comparison purposes, King *et al*.[6] held similar ONC using the fluidized bed where the total gas flow rate of NH_3, CO_2, and N_2 at 570 °C was equal to 1.5 m^3/h for 4 to 6 hours.

Usually, the increased surface toughness comes from the nitrogen and carbon in the diffusion layer. The tribological properties are also limited by the plastic deformation of the substrate material that could result in eventual coating failure[7]. Therefore, the type of steel used for thermochemical treatment is not a matter of indifference. Akbari *et al*.[8] stated that the response of tool steel to a thermochemical process depends not only on the alloy composition but also on the initial microstructure acquired as a result of the preliminary heat treatment. Other authors[9] declared that in the case of alloyed tool steels widely employed in the manufacturing of cutting and forming hot working tools, chromium is the dominant alloying element. The Cr-Mo-V containing tool steels exhibit a high level of resistance to thermal shock and thermal fatigue, good high-temperature strength, excellent toughness, ductility, and hardenability[10]. Although there is a large number of published works on nitro-carburizing of tool steels, little has been reported on the effect of the chemical composition of appropriate heat-treated and ONC tool steels on the microstructure, phase composition, hardness, layer depths, and scratch resistance. The study focuses on reactive nitrogen and carbon diffusion in four common tool steel grades for dies and molds. The differences and similarities in the microstructure, morphology, chemical, and phase composition of the compound and diffusion layer are related to the final tribological properties of the steels.

2 Experimental Procedure

2.1 Materials, heat and thermochemical treatment, samples preparation

Four different steel grades - AISI H10 (DIN 1.2365 EN 32CrMoV12-28, 3Х3М3Ф), AISI H11 (DIN 1.2343, EN X37CrMoV5-1,4Х5МФС), AISI H21 (DIN 1.2581, EN X30WCrV9-3, 3Х2В8Ф) and AISI D2 (DIN 1.2379, EN X153CrMoV12, H12MF) with the composition shown in Table 1, were subject to vacuum ONC process. The samples were used in quenched (in agitated mineral oil) and tempered condition which was obtained by conventional heat treatment. The heat treatment parameters were indicated in Table 2. The hardness of the quenched-tempered steel samples before the vacuum ONC process was in the range of H10 – 46 ± 0.71 HRC, H11 - 52.1 ± 0.37 HRC, H21 - 42.8 ± 0.75 HRC and D2 - 52.2 ± 0.6 HRC. The subsequent second tempering step was conducted together with the thermo-chemical treatment.

Before the thermochemical process, the steel samples were ground, mirror polished (Ra ≈ 0.08 - 0.10 μm), lapped, and degreased. The oxy-nitrocarburized layers were formed by a vacuum cycling process shown in Fig. 1. The process was carried out in an industrial installation. More details about the process parameters were discussed elsewhere[11].

2.2 Characterization

Cross-sections of the oxy-nitrocarburized samples were prepared by conventional metallographic techniques. Light optical microscopy (LOM) was performed by using a Neophot 21 (Zeiss, Jena) microscope after etching the samples with Murakami reagent (10 g $K_3Fe(CN)_6$, 10 g KOH, 100 ml H_2O). An oil immersion objective for reflected light was

Table 1 — Chemical composition (in wt%) of the steel samples before the ONC process.

Element	C	Si	Mn	Cr	Mo	V	W	P	S	Fe
H10	0.332	0.52	0.409	3.57	3.73	0.70	0.114	0.023	0.0099	Bal.
H11	0.36	1.18	0.423	5.38	1.32	0.33	0.034	0.034	0.0051	Bal.
H21	0.292	0.436	0.373	2.57	0.053	0.212	8.38	0.022	0.013	Bal.
D2	1.51	0.275	0.386	13.14	0.61	0.203	0.04	0.021	0.0075	Bal.

Table 2 — Preliminary heat treatment of the steel samples.

Heat treatment	H10	H11	H21	D2
Quenching temperature (°C)	1030±10	1030±10	1120±10	1040±10
Soaking time (min)	10	10	10	10
Tempering temperature (°C)	540±10	540±10	540±10	540±10
Soaking time (min)	60	60	60	60

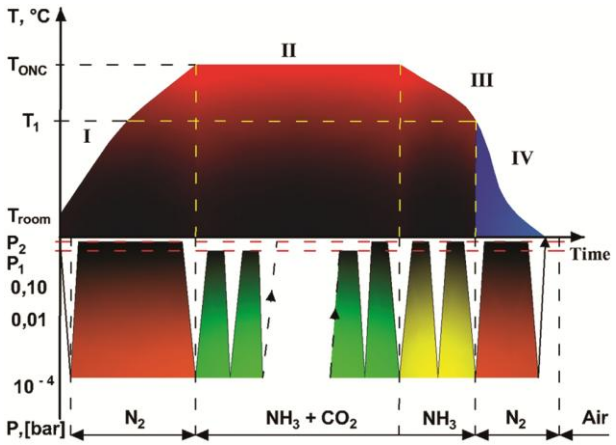

Fig. 1 — A model scheme of a cycling gas flow vacuum ONC process. T_{ONC} is equal to 560-570 °C, while T_1 is 400 °C; I – heating; II – saturating; III – cooling in the furnace; IV – cooling outside the furnace; P_1 = 0.8 bar (for the diffusion layer formation); P_2 = 1 bar (for the compound layer formation).

used. The metallographically prepared sections after etching with Nital (3% solution of concentrated HNO_3 in absolute ethyl alcohol) were also used for scanning electron microscopy (SEM) analysis. Micrographs of ONC samples were taken by JEOL JSM-5510 (Japan) with an accelerating beam voltage of 10 kV. The surface morphology and chemistry of the samples was also investigated by using SEM - LYRA I XMU, Tescan, equipped with energy dispersive spectroscopy (EDS – Quantax 200, Bruker) under an accelerating beam voltage of 20 kV. All samples were mounted on epoxy resin.

For phase identification, X-ray diffraction (XRD) was performed on the top surface of the samples by using URD-6 diffractometer with Fe-K_α line-focused radiation applying Bragg-Brentano geometry. The diffractograms were analyzed over a 2θ range of 30° to 120° degree with a step size of 0.05° 2θ and a continuing time of 2.5 sec/step. The Fe-K_α tube voltage and current were 30 kV and 20 mA, respectively. XRD Match!3 software was used to determine the phases and present the results.

The main elements participating in the ONC process – Fe, Cr, Mo, Si, W, V, N, C, and O were determined in depth of both layers by glow discharge optical emission spectroscopy (GDOES- LECO GDS-850A). Excited by DC voltage, Ar ions sputtered approximately 12.56 mm^2 areas. The measurement conditions used were 3.2 mbar, 20 mA, and 800 V.

Surface roughness parameters were determined by using Telidata-2000-1 contact profiler with sensing element – diamond needle. Five cut-offs of 0.8 mm were measured and the average values were reported. A Vickers Hardness tester 432 SVD by Wilson-Wilpert Instruments, Instron Company, was used for the hardness measurements of the steel according to the standard ISO 6507-1. In order to compare the microhardness changes, researches were made on the top and cross-sections of each sample (H10, H11, H21, and D2) after ONC with a load of 100 g and dwell time of 15 s by using microhardness ПМТ-3 (ПОМО) tester. The distance between the indents was equal to 20 μm.

Scratch tests were performed on the top surface of the samples with a CSM REVETEST Scratch Macrotester equipped with a Rockwell diamond indenter with a 200 μm tip radius. Progressive load scratching mode with a normal force range of 0N to 100N was used in the experiments at a speed of 10 N/mm. The scratch track was evaluated by using optical methods for each scratch and by means of digital-signal records of the coefficient of friction (μ), tangential force (F_t), and acoustic emission (AE) fluctuations. LOM of scratch tracks was performed by utilizing a Nikon microscope without etching the samples. To ensure the comparability of survey results for all samples, one and the same

magnification was applied. 14-megapixel digital camera was adapted to the microscope and used for the image acquisition.

Both scratch hardness (H_S) and plane strain fracture toughness (K_{IC}) that measures the resistance to cracks growth until fracture of the surface layer, were calculated according to Eqs (1 & 2) proposed by Hasan *et al*.[12] and Akono *et al*.[13], respectively.

$$Hs = \frac{8.F_N}{\pi.W^2} \quad \ldots (1)$$

where F_N is a normal force at maximal loading (100 N) and W is the residual width of the scratch after unloading.

$$K_{IC} = \frac{F_t}{(2.P.A)^{1/2}} \quad \ldots (2)$$

where F_t is a tangential force at a certain value of the normal load where the first crack occurs (L_{c1}); P is the perimeter and A is the area under the conical indenter.

3 Results and Discussion

The phase equilibrium for medium and high alloy steels seems significantly different from that of pure iron. In the tempered martensite structure of alloyed tool steels with nitride forming elements, the dissolved nitrogen interacts not only interstitially with ferrite but also reacts with the carbides to form nitride precipitates or carbonitrides. Therefore, the usage of similar to Lehrer diagram three-dimensional isothermal diagram of Fe-N-C system could be misleading when applying it to the complex microstructures (multi-component, multi-phase diffusion equations) of alloyed steels. Consequently, before the experiments, some thermochemical calculations were done to estimate the possible reaction products during the process that has both "nitriding" and "carburizing" potentials in a gas mixture of NH_3/CO_2 at 0.8 bar, and 570 °C. First, some metastable diagram calculations, which belong to Fe-N-C and Fe-N-C-X systems (X = Cr, Mo, W), were performed by using "phase diagram" module of FactSage 7.1 Thermochemical Software[14]. Then, the effect of oxygen on the carbonitride phases was investigated by using the same module.

In the calculations, the SGTE2014 database was selected to describe the liquid and solid phases in the system. The isothermal section of the metastable Fe-N-C ternary phase is shown in Fig. 2 a. When N/C ratio level is high, which corresponds to the high

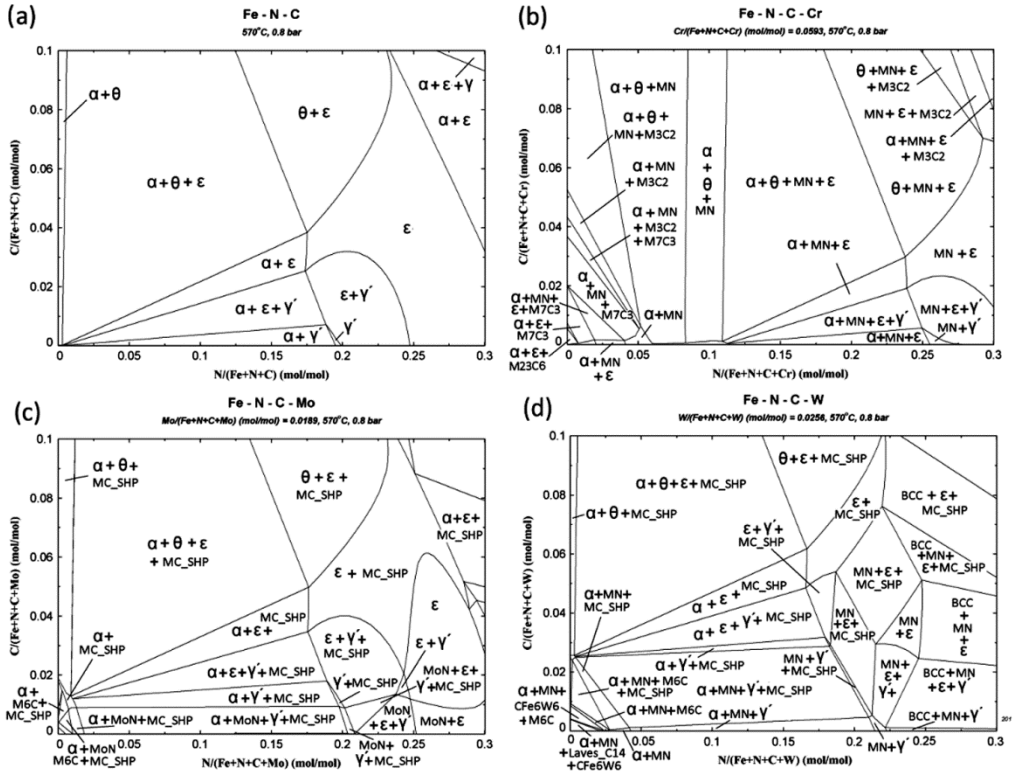

Fig. 2 — Metastable phase diagrams of (a) Fe-N-C, (b) Fe-Cr-N-C (5wt% Cr), (c) Fe-Mo-N-C (3wt% Mo) and (d) Fe-W-N-C (8wt% W) calculated by FactSage at 570 °C and 0.8 bar.

ammonia content in the system, a mixture of γ` (M_4N) and ε (HCP_A3) phases or only single ε (HCP_A3) phase occur as the possible compound layer on an iron substrate. However, when N/C ratio is low, the development of these phases is suppressed with θ (cementite) formation, corresponding to a higher CO_2 content in the gas atmosphere. Fig. 2b reveals that when 5 wt.% Cr (0.0593 at %) is added to Fe-N-C system, MN (FCC, (Fe,Cr)N) phase coexists with γ` (M_4N) + ε (HCP_A3) or only with ε (HCP_A3) at rich nitrogen zone. In addition to cementite, M_3C_2, M_7C_3, and $M_{23}C_6$ are three carbide phases predicted to be also stable at different concentrations of carbon. When Mo is selected as a second metal (3 wt% Mo) to the Fe-N-C system, in addition to γ` and ε phases, MoN and/or Mo(C,N) (MC_SHP) formations emerge in rich nitrogen zone (Fig. 2c). The calculation result of a similar phase diagram with 8 wt% W represents the possible carbide phases to be Mo_6C, Fe_6W_6C, W(C,N) (MC_SHP), and cementite (Fig. 2d). As the nitrogen content in Fe-Mo-N-C system increases, the nitride formations were predicted as MN, (Fe,W)(N,Va) (BCC), ε, and γ`.

The calculation result on the oxidation behavior of ε (HCP_A3, with 1.5 wt% C and 10 wt%N) in Fe-N-C system during cooling is represented in Fig. 3. The result shows that the unique oxide phase is a spinel solid solution (*i.e.* Fe_3O_4) which develops from the single ε (HCP_A3) at 570 °C and 0.8 bar. As the temperature decreases, in addition to ε and spinel, γ`(M_4N) and α-iron phases could form, respectively.

The characteristic features of the cross-sections of the vacuum ONC tool steels are shown in Fig. 4, 5, and 6. The surface carbides and carbonitrides of all specimens were readily attacked by the Murakami reagent and appeared dark. The compound layers

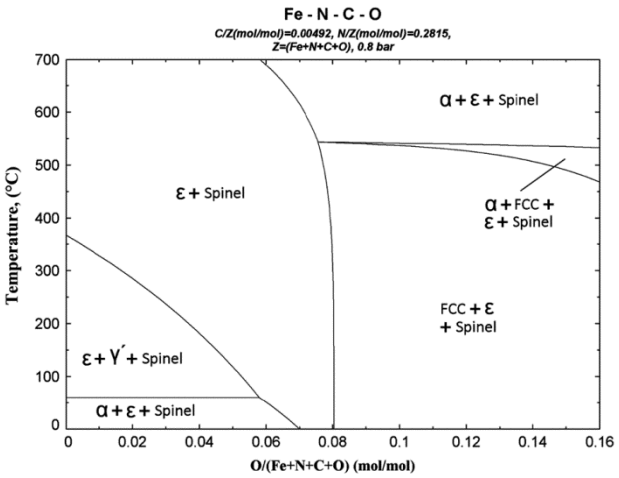

Fig. 3 — The oxidation behavior of Fe-N-C system (1.5 wt% C and 10 wt% N) with temperature calculated by FactSage at 570 °C and 0.8 bar.

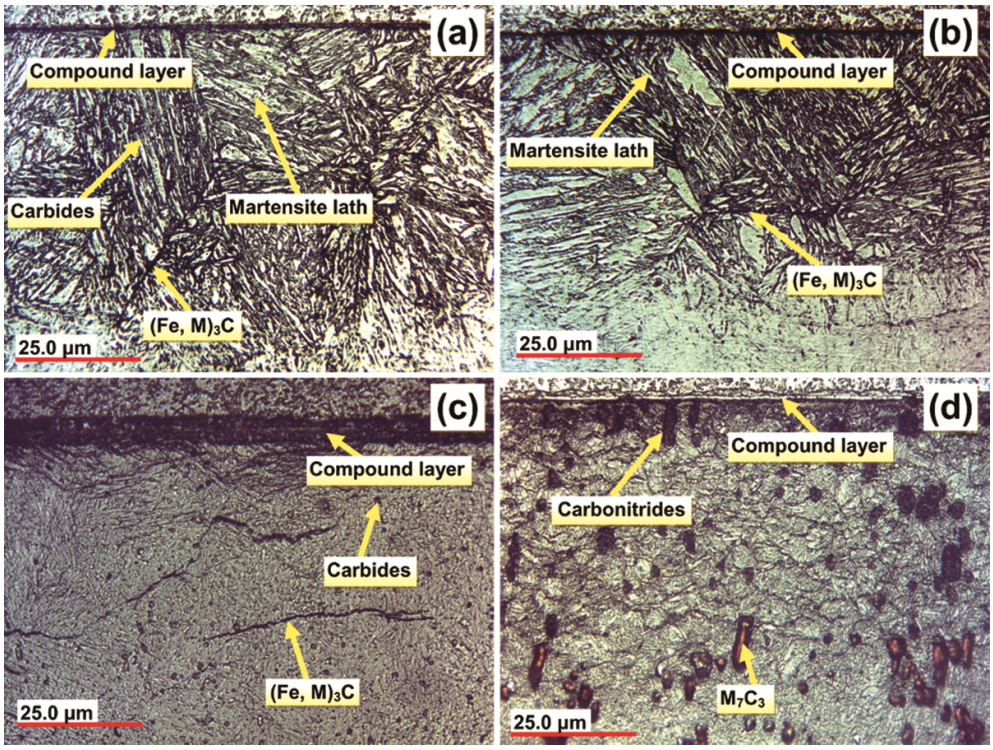

Fig. 4 — Representative optical micrographs of the cross-sections of the ONC steels, etched in Murakami: (a) H10, (b) H11, (c) H21 and (d) D2.

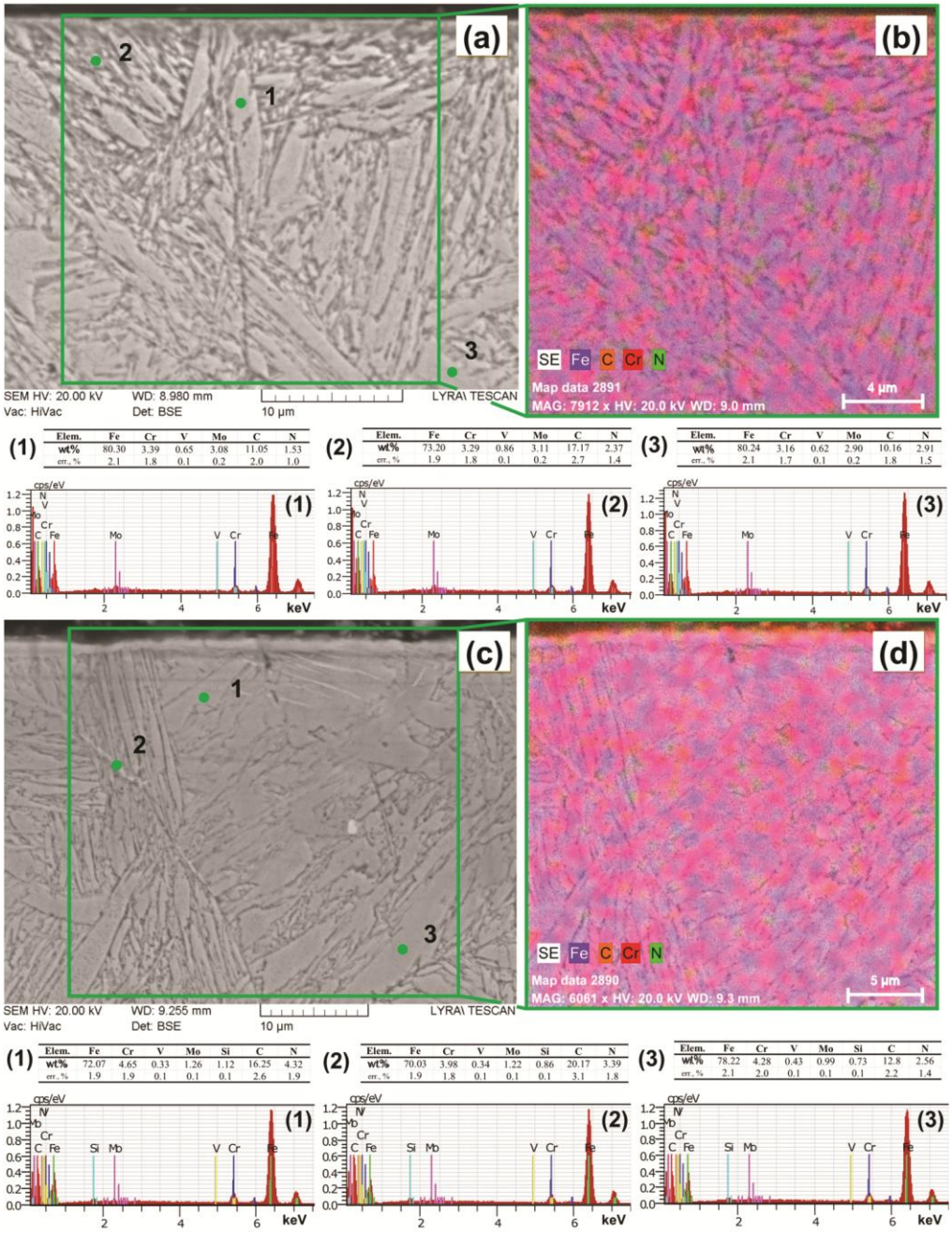

Fig. 5 — Representative cross-section SEM micrographs (BSE mode), (a & c) and elemental mapping of Fe, C, N, and Cr (b & d) of ONC steels etched in Nital: a, b) H10; c, d) H11. The chemical composition of points 1, 2 and 3 are shown below the corresponding images.

were not clearly seen by optical microscopy due to their small thickness. The diffusion layer in an ONC steel could, in practice, be divided into three sub-layers: surface, matrix, and transitional area. The region directly below the surface sublayer (matrix) was distinguished by the greater sensitivity to Murakami etching, appearing darker than the transitional area. The innermost located area looked paler towards the core material and mainly contained a solid solution of nitrogen in the tempered martensite with similar microstructure as the untreated samples (not shown here).

The cross-section micrographs of ONC H10 steel (Fig. 4a) revealed the distinct prior austenite grain boundaries in the diffusion layer after Murakami etching. Within the grains, the lamellar morphology of coarse tempered martensite could be seen. A similar morphology was observed for ONC H11

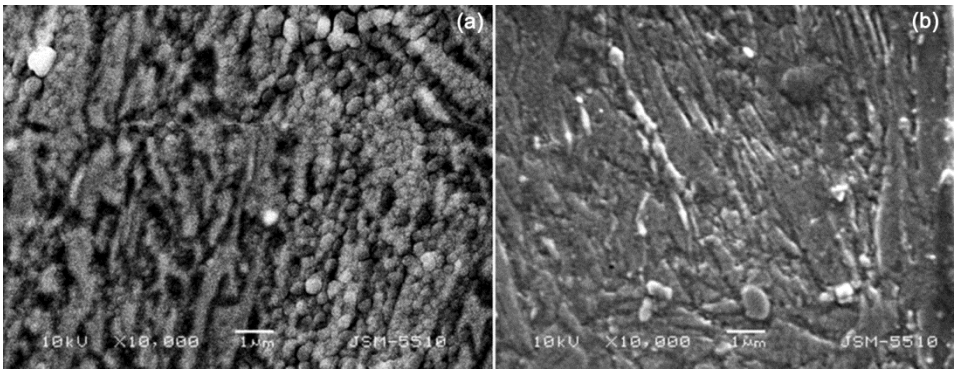

Fig. 6 — Representative SEM micrographs (SE mode) of the diffusion layers of (a) ONC H10 and (b) ONC H11 steel.

(Fig. 4b). The inspections of ONC H21cross-sections (Fig. 4c) indicated spherical dark-looking carbide particles - Fe_6W_6C or M_6C, as predicted in the thermochemical calculations in obviously finer martensite structure. Elongated nitrocarbide phases along some grain boundaries were seen merely parallel or inclined less than 45° with respect to the surface. Underneath the compound layer, where the concentration of nitrogen and carbon was the highest (Fig. 9c), coarser phases were formed within the diffusion layer (Fig. 4c). The gradient Murakami staining of ONC D2 steel (Fig. 4d) allows all phases in the diffusion layer to be clearly defined. The former primary carbides had become darker stained phases in the diffusion layer. The carbides deeper in the diffusion layer were not significantly affected in size and dispersion. Along the grain boundaries that were nearly parallel with respect to the surface, coarse tubular phases were distinguished.

The back scattered SEM images with marked places of analysis of the concentration of chemical elements are shown in Fig. 5 (a & b) and Fig. 6. Figure 5 depicts the backscattered SEM micrographs of ONC H10 and H11 steels where their thin compound layers looked free of pores. This observation emphasizes the substantial difference between a compound layer formed during vacuum ONC processes and that produced for example on M2 substrate using a conventional gas process with similar gas phase and at similar temperature[15]. The process was held in a fluidized bed for 4 hours and as a result, 18 μm-thick and a highly porous white layer was observed. The lamellar structure of H10 steel with increased lamellar spacing observed near to the surface (Fig. 5a, point 2) revealed higher carbon content as compared with the near-core zone (point 3). The degree of precipitation at the grain boundaries of the lamellar structure of ONC H10 steel (Fig. 5b) seemed higher than that of ONC H11 steel where Cr and C tend to be predominantly located within the tempered martensite laths (Fig. 5d). This fact was confirmed by the detected higher Cr content in the martensite laths (marked points 1 and 3) as compared to that at the boundary point 2 measured in ONC H11 steel. This phenomenon Zhang *et al*.[16] explained by the delayed decomposition of martensite when the carbon content in the steel was increased. The interstitial carbon reduces the number of available nitrogen sites in the tempered martensite lattice. Additionally, Nayebpashaee *et al*.[17] suggested that during plasma nitriding the distorted bct structure of martensite decreased the available spaces in the lattice for nitrogen and the compressive residual stresses accumulated after quenching and tempering in the normal direction to the surface decreased the space between the parallel atomic spaces and hindered substantially the atomic diffusion. Therefore, the diffusional motions of nitrogen atoms are hindered and they have been trapped in Fe-Me(Cr,V)-N configuration without forming many alloy nitrides, thus impeding the nitrogen diffusion in depth. Carbon pushed by the nitrogen atoms formed a lamellar grain boundary $(Fe,M)_3C$ (Fig. 5b, point 3). It is obvious that the volume diffusion of nitrogen in the matrix of ONC H11 was the active process forming fewer nitride precipitations at the grain boundaries and a shallower diffusion layer (that will be encountered later). In contrast to H11 steel, the low-carbon containing H10 sample separated cementite earlier in the tempering process that was transformed into Fe and Cr containing spherical carbonitrides shown in Fig. 6. Similarly, King *et al*.[18] discovered that the fine internal lath cementite could dissolve under the influence of nitrogen diffusion while the coarser boundary cementite could act like nuclei for MeN formation.

In the diffusion layer of ONC H21 steel (Fig. 7a), Mo- and W-rich carbides appeared bright while Fe and Cr-rich precipitates near the end of the compound layer appeared darker. In contrast to the other three specimens – ONC H10, H11, and D2 where the compound layers were very thin, ONC H21 showed thicker and dense nitride zone forming smooth transition interface between the compound and diffusion layers. The chemical composition determined at the brighter phases (points 2 and 3) suggests that these were alloy carbides rich in W, Fe, and with low Cr content. Although these carbides appeared untransformed, they could be identified within both compound and diffusion layers (Fig. 7a). In the white layer, the nitrogen concentration was the highest while in the diffusion zone N content locally increased up to 6.8 - 8.6 wt%. Underneath the compound layer where both nitrogen and carbon concentrations were high and the driving force for the discontinuous coarsening was maximal, more abundant and coarse carbide precipitates within the finely tempered martensite (Fig. 7a, point 1) were observed. The effect of the upward diffusion in GDOES analysis (Fig. 10) also evidenced that fact.

SEM micrographs of ONC D2 steel (Fig. 7b) reveal a compact compound layer without pores. The darker looking (Cr,Fe)(N,C) phases (point 2) were part of the diffusion layer behind the transformation front where nitrogen atoms replace carbon atoms in the primary $(Cr,Fe)_7C_3$ carbides. As seen in Fig.8, the primary carbides formed nitrogen-saturated areas, where a certain part of carbon was substituted by nitrogen. Nitrogen was predominantly concentrated in

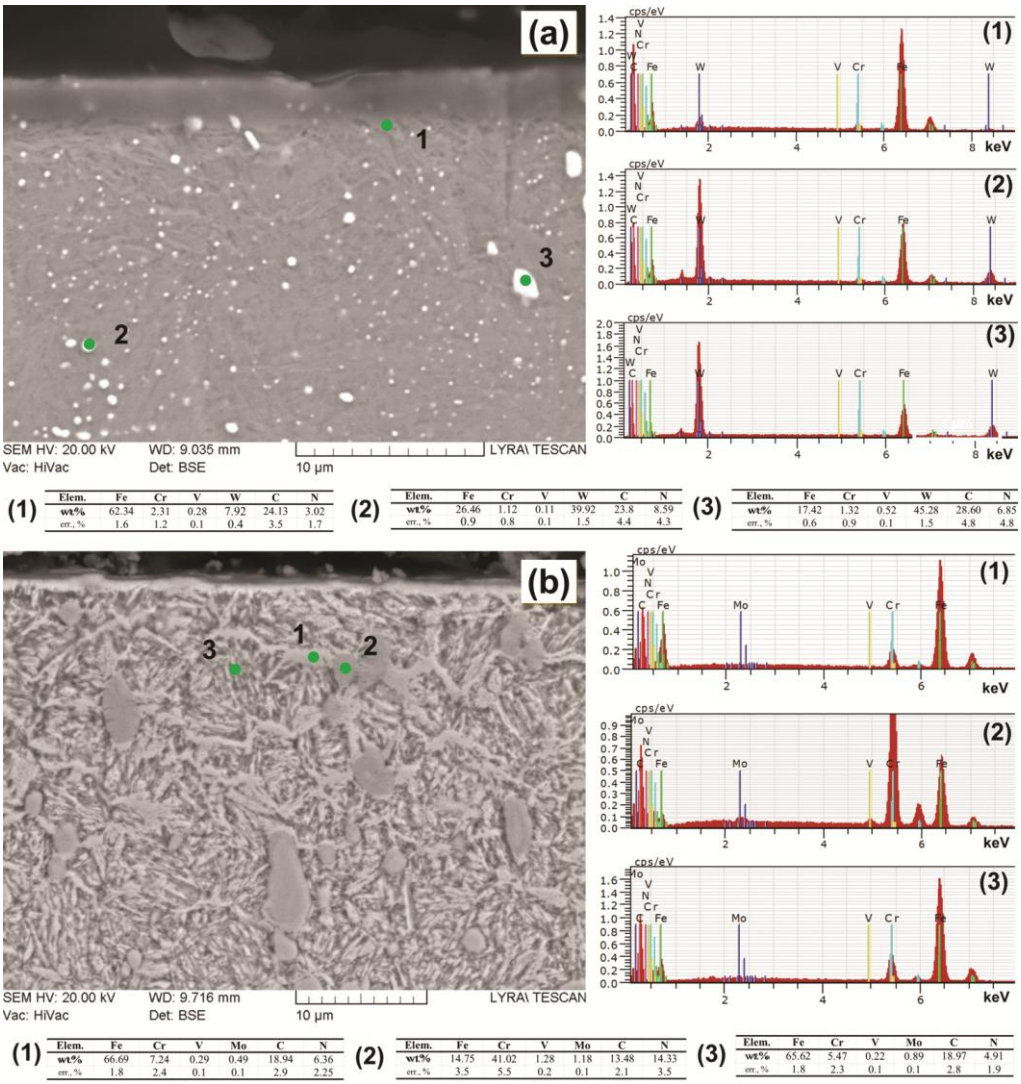

(1)	Elem.	Fe	Cr	V	W	C	N
	wt%	62.34	2.31	0.28	7.92	24.13	3.02
	err., %	1.6	1.2	0.1	0.4	3.5	1.7

(2)	Elem.	Fe	Cr	V	W	C	N
	wt%	26.46	1.12	0.11	39.92	23.8	8.59
	err., %	0.9	0.8	0.1	1.5	4.4	4.3

(3)	Elem.	Fe	Cr	V	W	C	N
	wt%	17.42	1.32	0.52	45.28	28.60	6.85
	err., %	0.6	0.9	0.1	1.5	4.8	4.8

(1)	Elem.	Fe	Cr	V	Mo	C	N
	wt%	66.69	7.24	0.29	0.49	18.94	6.36
	err., %	1.8	2.4	0.1	0.1	2.9	2.25

(2)	Elem.	Fe	Cr	V	Mo	C	N
	wt%	14.75	41.02	1.28	1.18	13.48	14.33
	err., %	3.5	5.5	0.2	0.1	2.1	3.5

(3)	Elem.	Fe	Cr	V	Mo	C	N
	wt%	65.62	5.47	0.22	0.89	18.97	4.91
	err., %	1.8	2.3	0.1	0.1	2.8	1.9

Fig. 7 — Representative SEM micrographs (BSE mode) of a cross-section of the ONC steels, etched in Nital (a) H21 and (b) D2. The chemical composition of points 1, 2, and 3 are shown next to the corresponding images.

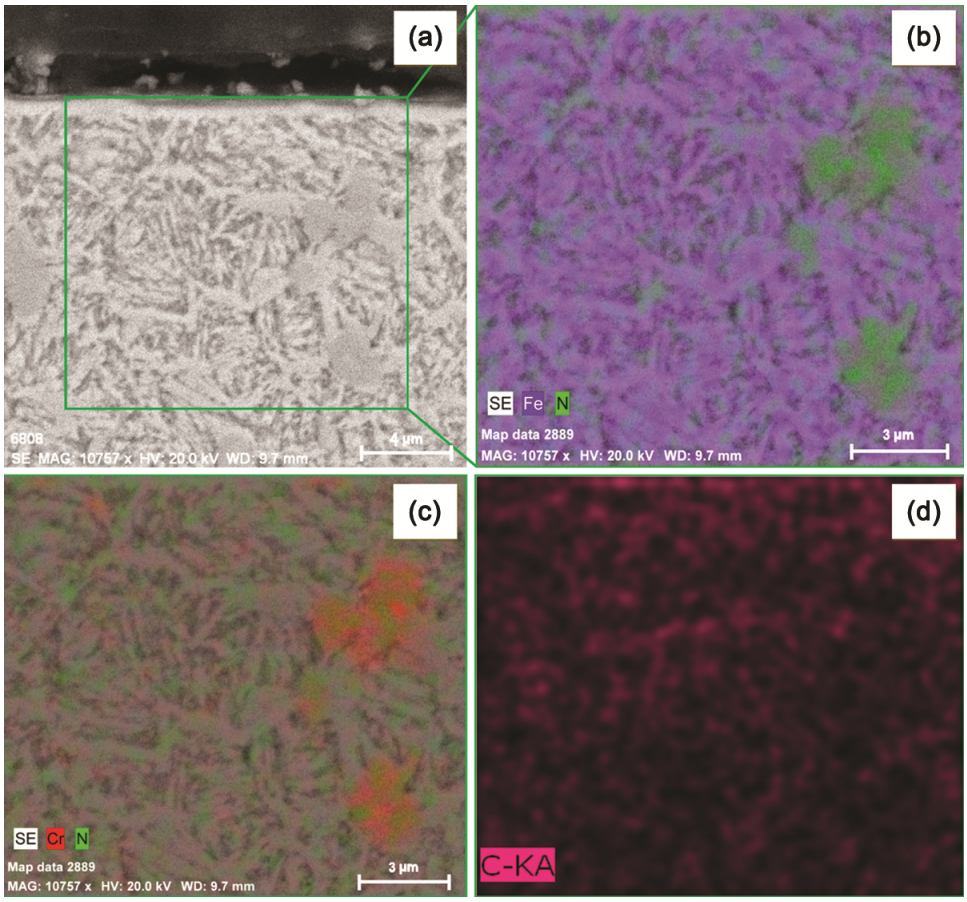

Fig. 8 — Maps of the distribution of some chemical elements of ONC D2 steel: (a) SEM image, (b) elemental mapping of Fe and N, (c) elemental mapping of Cr and N and (d) elemental mapping of C in the microstructure.

the zone of primary carbides and less in the tempered matrix where it formed smaller-sized Fe and/or Cr-containing precipitates. Cr atoms from the primary carbides tended not to move from their initial positions, while C redistributed more homogeneously towards the diffusion front at the grain boundaries. The reaction of Cr with N caused increased hardness values of the transformed primary carbides that reached values of 1637.25 ± 21.5 HV0.05 as opposed to the pure carbide phases in the substrate that showed lower hardness – 1190.25 ± 13.5 HV0.05. The deeper located primary carbides at a distance more than 250 µm from the surface contained Fe 40.69 ± 1.1 wt%, Cr 40.30 ± 6.1 wt%, V 1.34 ± 0.2 wt%, Mo 1.30 ± 0.1 wt%, C 14.66 ± 2.3 wt%, and N 1.71 ± 1.1 wt%. As seen in Fig. 5d, despite their size, full transformation of the primary carbides occurred up to about 50 µm depth of ONC D2 substrate, in contrast to earlier reported work of King *et al.*[18] on ONC in fluidized bed of D2 steel where the authors found partially transformed carbides in the first half or two-thirds of the diffusion layer and this ratio was not altered if CO_2 or no CO_2 was added. Similar results establishing partially transformed carbides were observed after vacuum nitriding of D2 for 3 hours at 560 °C[19]. The aforementioned difference could be attributed to the increased nitrogen potential during the vacuum ONC as well as the long process duration.

Thick elongated near parallel to surface phases forming white "nets" were found to be mainly Fe-and Cr-containing carbides with small N concentration in them (Fig. 7b, point 1). The primary carbides' transformation triggered $(Fe,M)_3C$ or other carbide precipitation at the grain boundary because the binding energy of Fe-N is higher than of Fe-C. Psyllaki *et al.*[20] discovered that during liquid nitrocarburizing these surface orientated structures acted as diffusion barriers limiting the thickness of the diffusion layer by decreasing the process kinetics. The other elements like Mo and V with low intensity were homogeneously distributed in the diffusion layer (not shown here).

The XRD patterns of all ONC steels (Fig. 9) confirmed that the diffraction peaks of the compound layer corresponded to monophase ε-carbonitride. According to Sohi *et al.*[21], the heterogeneous γ` and ε structure has inherited high internal stresses arising from the phase boundaries that make the compound layer friable and brittle. The intensity and number of ε-phase peaks increased in the case of ONC H11, and especially in that of ONC H21 and D2 steels in contrast to ONC H10 where only (111)-orientated ε reflections were present. Hence, the lower carbon and increased Mo and V content in the tempered martensite structure of ONC H10 steel result in high nitrogen consumption in the diffusion layer that diminishes the compound layer thickness and directly collaborates with the microstructure observations.

The carbide and nitride diffraction peaks of ONC H21 and D2 steels were not well distinguished which can be ascribed to the high background resulting diffuse scattering of the sample surface. Another reason for this effect Rocha *et al.*[22] found in a superimposition of diffraction lines. In terms of α-(110) peaks, all of them were shifted to lower angles because of the presence of nitrogen introduced into the solid α-Fe(N,C) solution. Both α-(200) and α-(211) reflections were not clearly seen or completely disappeared which phenomenon Ueda *et al.*[23] explained with the precipitation of small coherent particles within the matrix of plasma-treated H13 steel.

As predicted from the thermodynamic calculations and confirmed by the XRD examination, the

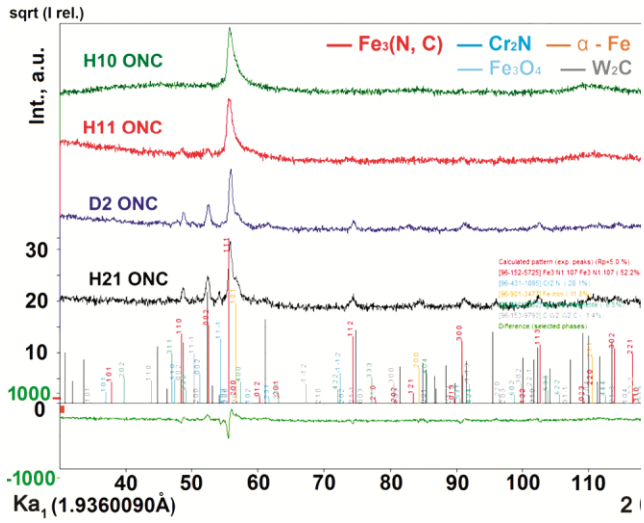

Fig. 9 — Bragg-Brentano X-ray patterns from the surface of oxy-nitrocarburized steels. ε (hcp, $Fe_3N_{1.7}$), Cr_2N (trigonal (hexagonal axes)), α (expanded bcc), W_2C (trigonal (hexagonal axes)) and Fe_3O_4 (fcc) are indicated together with their HKL values.

increased oxygen activity triggers magnetite phase growth within the ε-phase structure and makes the samples' surface to appear silver-gray. Hong *et al.*[24] noticed that the magnetite formation was favored at a high partial pressure of H_2 which exists during the vacuum ONC process while Zlatanovic *et al.*[25,26] confirmed that the magnetite formed during pulsed plasma-oxidation of nitrided steels was effective against wear and corrosion because of its compact structure, low friction coefficient, and chemical stability.

The concentration profiles of ONC specimens (Fig. 10) displayed smoothly varying gradients of all examined elements. The nitrogen profiles of ONC samples pointed out that the surface nitrogen content was close to 8-13 wt% for all steels except H21 where N concentration reached about 20 wt%. The nitrogen profiles confirmed thinner compound layers (0.7 - 1 μm) in the case of ONC H10, H11 and D2 steels and somewhat thicker layer for ONC H21 (about 4.5 μm) which had been previously determined by microstructure analysis. Without taking into account the differences in the compound layer thickness, oxygen peak positions were located at similar distances with respect to the surface (0.4 - 0.5 μm) where oxidation of ε-phase occurred. Cr content was found to increase in the oxygen-containing area because of the high oxidation potential of the element. Subsequently, a substitution of Fe by Cr in $(Fe,Cr)_3O_4$ is reasonable to be expected within the surface zone.

P. Cavaliere *et al.*[27] observed that the element diffusion during nitriding was faster when the content of alloying elements was higher. As seen from the results of this study, the higher the concentration of the alloying elements, the higher the driving force for the coarsening reaction of precipitates especially in ONC D2 and H21 steels. Despite the lowest levels of Cr among others, a stronger Cr concentration peak was found in ONC H21 steel. The non-homogenous distribution of Cr in contrast to Mo and V indicates that the former participated in the formation of larger near-surface precipitates. The carbon increment under the surface was the highest for ONC H10 (about 2.6 wt%) and the lowest (average 1.4 wt%) but increased at greater depth in the case of ONC H21 steel. In contrast, carbon fluctuations underneath the surface of ONC H11 and D2 showed similar trends and values.

The effective case thickness of the diffusion layer was calculated as the case hardness values reached the substrate hardness and 50 HV was added[28]. As expected, under the same ONC temperature and

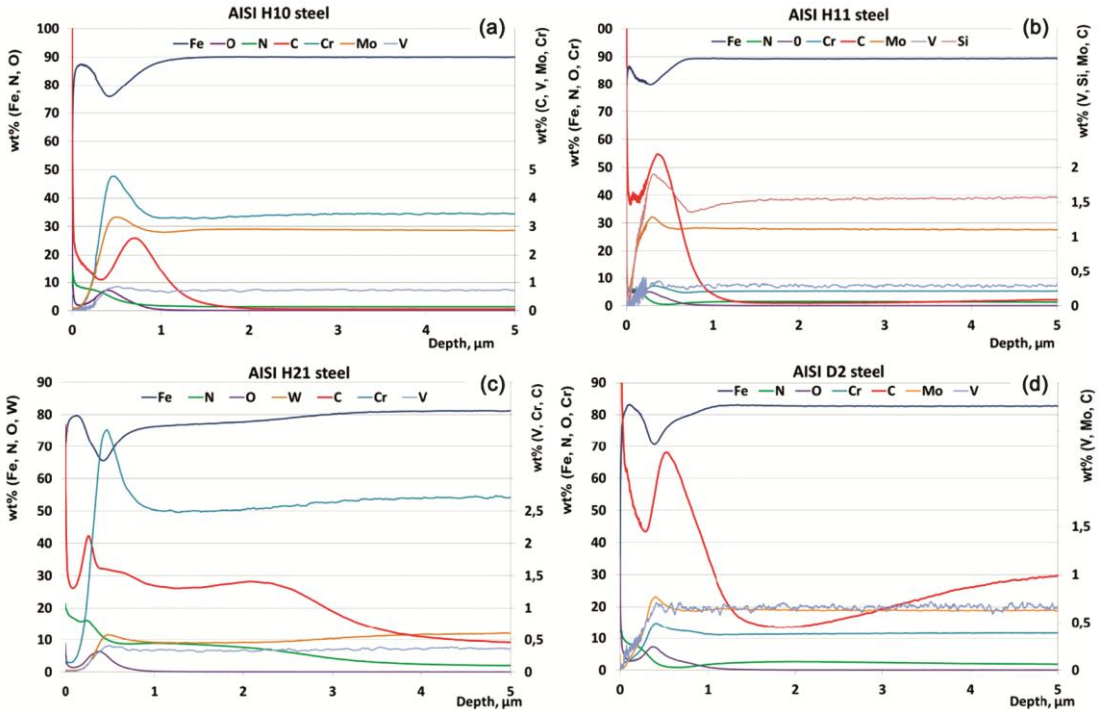

Fig. 10 — Concentration–depth profiles from the GDOES of oxy-nitrocarburized steels: (a) H10 steel, (b) H12 steel, (c) H21 steel, and (d) D2 steel. The distribution of the elements from the substrates: Fe, Cr, Mo, V, Si, W and metalloids N, C, and O are presented.

duration, the maximum subsurface hardness was reached for ONC D2 steel (Fig. 11). However, D2 microhardness decreased gradually within the shallower diffusion layer. For both ONC H10 and H11, the cross-sectional hardness dropped sharply from the outermost zone of the diffusion layer towards the substrate. Similar values of microhardness and diffusion layer depth were declared by Fares *et al.*[29] for 8 hours salt bath nitrocarburized at 580 °C of H11 and H13 steels, with the sole difference that the compound layers were porous and they yielded significantly lower surface hardness values. The highest hardness values of ONC H21 steel were located at about 30 µm below the surface while the near-surface hardness was significantly lower due to the coarsening of precipitates. The diffusion layer hardness of ONC H21 followed plateau-shape behavior and it decreased more slowly with increasing the distance from the surface. The differences between the top hardness measurements (Table 3) and cross-section microhardness results (Fig. 10) concerned the distance from the surface where the maximum hardness was maintained.

The surface roughness values after ONC of the samples, shown in Table 3, were slightly affected by the treatment that could be attributed to the small thickness of the compound layers. Slightly higher surface roughness values were found for ONC H11

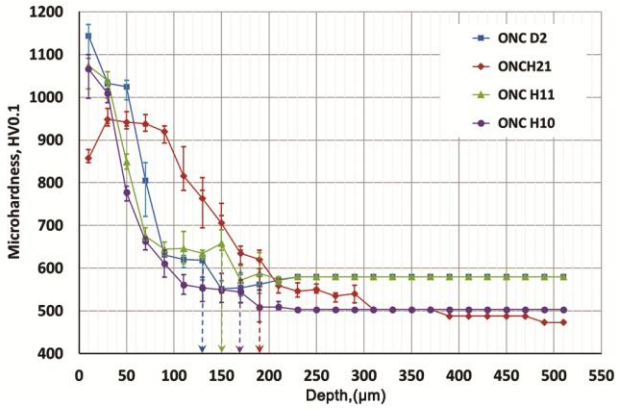

Fig. 11 — Distribution of the microhardness in depth of ONC samples. The diffusion layer depth of each sample is calculated by adding 50 HV to the substrate hardness. Error bars: standard deviations.

and D2 steels corresponding to their high surface hardness and the volumetric lattice expansion associated with in-depth atoms' diffusion. As the coefficient of friction (µ) depends on the surface roughness, layers' structure, and lubricated conditions[16], the small and close values of the initial surface roughness suggest that the starting surface conditions will be rather similar at the beginning of the scratch test. Then, the determinative factor remains to be the difference in the structure and properties of steels.

The calculated parameters obtained from the scratch test results are summarized in Table 4. ONC H10 steel demonstrated the lowest scratch hardness (H_S) while the rest ONC samples showed similar H_S values. The calculated fracture toughness (K_{IC}) of ONC H10 was equal to 10.11 MPa.m$^{1/2}$ at L_{c1} (F_N = 23.62 N) which was higher than that of ONC H11. The lower K_{IC} value of H11 at L_{c1} = 22.68 N indicated that the steel was more prone to brittle fracture. Despite the thicker compound layer, lower K_{IC} values were determined for H21 as compared with D2 steel. For ONC D2 steel, the value of K_{IC} was the highest which could be attributed to the reduction of micro-cracking tendency due to the increment of diffusion layer hardness because of the precipitation of hard carbonitrides and reduced residual stresses in the material.

F_t = f(F_N) diagram (Fig. 12a) established that F_t trends at low loading for both ONC and non-ONC

Table 3 — Surface roughness values, top surface hardness and depth of the diffusion layers produced after vacuum ONC of the tool steels.

Steel	Ra(μm)	Amplitude distribution		HSC	T_P(%)	Top surface hardness HV0.1	Diffusion layer depth (μm)
		Zonewidth (μm)	P_C (cm^{-1})				
H10	0.10±0.004	0.4	15	55	51.4	1146±32.86	≈ 170
H11	0.11±0.004	0.5	13	62	50.7	1158±26.83	≈ 150
H21	0.10±0.005	0.3	43	70	46.6	883±36.52	≈ 190
D2	0.11±0.007	0.4	56	33	43.5	1298±26.83	≈ 130

Ra is mean roughness, P_C is mean height of profile elements, HSC is high spot count and T_P is profile bearing length ratio.

Table 4 — Calculated values of the scratch hardness (H_S) of the substrates and ONC tool steels, critical failure point (L_{C1}), W is the residual width of the scratch after unloading at L_{C1} and fracture toughness (K_{IC}) at L_{C1}.

Parameter Steel		H_S at 100 N(GPa)	L_{C1} (N)	W at L_{C1} (μm)	K_{IC} at L_{C1}(MPa.m$^{1/2}$)
H10	Substrate	7.26	-	-	-
	ONC	12.00	23.62	99.33	10.11
H11	Substrate	7.54	-	-	-
	ONC	13.74	22.68	76.64	7.38
H21	Substrate	5.93	-	-	-
	ONC	14.16	44.52	93.23	13.14
D2	Substrate	8.58	-	-	-
	ONC	13.85	55.47	95.07	15.63

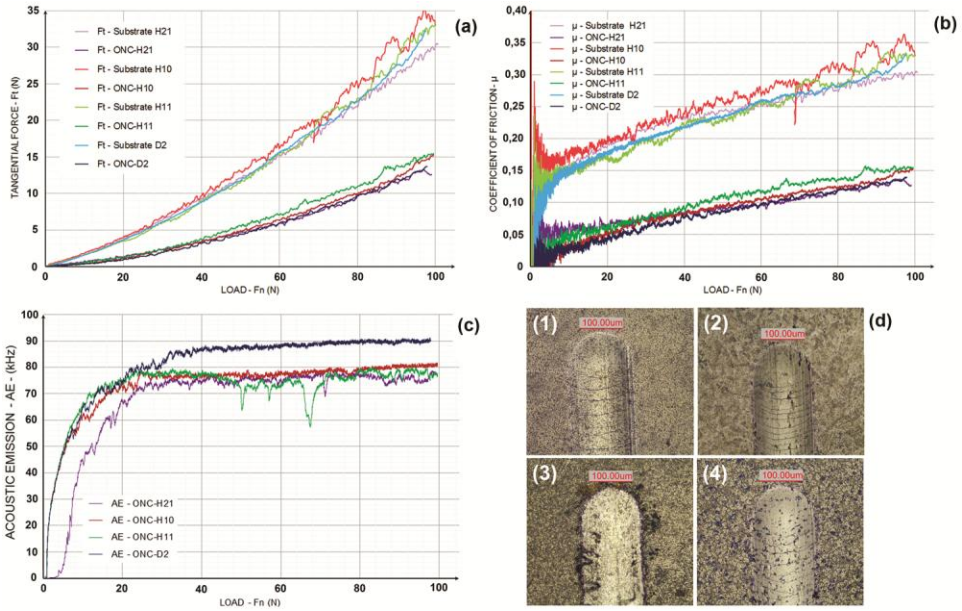

Fig. 12 — Comparison of the: (a) tangential forces (F_t),(b) coefficient of friction (μ),(c) acoustic emissions (AE) of all of the examined substrates and ONC steels during progressive 0 N to 100 N scratch test and (d) micrographs of each scratch track end of the ONC steel: (1) ONC H10 steel; (2) ONC H11 steel; (3) ONC H21 steel; (4) ONC D2 steel.

samples were similar in character and with the increase of F_N, the F_t fluctuations lead to changes in the tendency of curves. The most significant changes occurred in H10 substrate and minor amendments were found for F_t values of H21 steel at maximum load. Similar trends were seen after the vacuum ONC treatment. The highest F_t values were those of ONC H11 while the lowest values were set for D2 and H21 steels at a load of 100 N. All non-ONC specimens showed higher μ values (Fig. 12b) under scratch conditions. The highest was the μ-trend of H10 throughout the entire test while that of D2 showed the lowest values in the start-up phase of the test. In the comparative diagram, the range of μ changes of ONC tool steels was smaller as opposed to that of the substrates. The needle-like ONC martensitic laths tended to give as a lightly higher coefficient of friction than the ONC structures of H21 and D2 steels. At low loading, μ-trend of ONC H21 showed the highest fluctuations because of the lower sub-surface hardness but at the end of the test, both ONC H21 and D2 indicated the lowest μ values. The strengthened diffusion layer and substrate material resulted in preventing deep ploughing of the indenter thus reducing the scratch friction coefficient and increasing fracture toughness through improving the mechanical support of the compound by the diffusion layers.

AEs of ONC specimens released during the process of scratching (Fig. 12c) indicated an impressive range of high values for all samples with the exception of ONC H21 steel that showed initial lower fluctuations up to 26.84 N because of the collapsing effect under load. After this point up to the maximum load, ONC H10 and H21 followed a similar level of AEs (≈ 80 kHz and 77-78 kHz, respectively) while ONC D2 showed higher AE fluctuations. The initial AE signals of ONC D2, H10 and H11 were fairly stable up to 16.12 N because of the higher surface hardness. With the increase of load, AE of ONC D2 remained approximately constant at a value of ≈ 90 kHz mostly due to the fact that the diffusion layer was slightly plastically deformed up to the maximum load as confirmed by the scratch track end (Fig. 12d). Although at different kHz levels, AEs of ONC H10 and D2 steels showed maximum stability until the end of the test. In the case of ONC H11, AE fluctuations could be associated with hertz cracking of the plastically deformed material up to100 N load.

For all samples, the compound layer covering the surface was not fragmented up to 100 N normal force. Then, the enhanced wear resistance could be attributed to the presence of monophase ε-containing compound layer because Wen[30] claimed that its intermetallic structure allows sliding along the base plane thus reducing the amount of heat produced during friction. Because of the substrate deformation, the residual groove of ONC H10, H11, and D2 steels exhibited a tensile mode of transverse semi-circular cracking behind the indenter (Fig. 12d-1, 2, 4). However, the crack spacing of ONC H11 was smaller than that of ONC H10 and some additional crack bridging to the transverse cracks in the longitudinal direction were also seen in Fig. 12d (2 & 4). In all three cases, the difference in the lattice structure of the compound-matrix phases and the sharp transition between them induce strain incoherency and lattice defects (dislocations) occurring at the compound-diffusion layer interface which results in cracks formation under loading. In the case of ONC H21 (Fig.12d-3), after unloading the elastic-plastic behavior of the diffusion layer tended to deform some parts of the compound layer because of local substrate collapse causing small fractures in the upper layers. The higher thickness of the compound layer and the smooth transition between the zones improved the toughness of the nitride layer.

4 Conclusions

This work demonstrates that the tribological performance of ONC tool steels is directly related to the phase composition of the surface compound layer and the depth and composition of the diffusion layer while taking into account each phase volume, distribution, and hardness. With the exception of alloy nitrides and carbide phases, XRD and GDOES patterns revealed that the compound layer crystallinity and composition are largely similar for all samples so that the tribological behavior of ONC steels showed many similarities. Despite the use of CO_2 as a carbon-bearing source, the thin compound layer formed during vacuum ONC and the absence of near-surface porosity in both compound and diffusion layers suggested a lack of excess nitrogen absorbed at the surface or matrix/precipitates interfaces. Both effects could be attributed to the vacuum conditions of treatment. The nitride phases formed predominantly inside the grains of H11 steel gave rise to higher hardness, lamellar grain boundary carbides, and sharp layers transition that triggered increased internal stresses, excessive brittleness and earlier loss of structural integrity. In the case of ONCH10, the

transformed spherical precipitates located mainly at the grain boundaries together with the higher superficial nitrogen concentration as opposed to H11 steel provided residual stress relaxation and better scratch test performance. Despite the increased initial μ values because of the coarse and softer precipitates near to the surface of ONC H21 steel, μ and F_t values of the deeper located carbonitrides and disperse primary W-containing carbides approximated those of ONC D2 steel. The smooth N and C transition from the compound towards the diffusion layer down to approximately 4.5 μm in-depth increased the spalling resistance of the white layer of ONC H21 steel. The near-surface located fully transformed carbonitrides of ONC D2 steel retained the size and dispersion of primary carbides but increased their hardness. The former together with the precipitated coarse tubular carbides and nitro-carbides elongated merely parallel to the surface indicated the highest surface hardness, the lowest and most stable μ values, and a reduction of cracking tendency of the compound layer.

The thermochemical calculations presented as metastable phase diagrams accounting the low-pressure conditions, gas phase composition and tool steel composition provides a good prediction of the reaction products obtained after the vacuum ONC process. However, they do not account for the preliminary heat treatment and individual element interactions in the complex alloyed system as well as the phases' distribution and their sizes which appeared to be determinative for the tribological performance of ONC tool steels.

This work should be complete by examinations exploring the performance of compound layers of the vacuum ONC tool steels in a corrosive environment.

References

1 Riofano R M M, Casteletti L C, Canale L C F & Totten G E, *Wear*, 265 (2008) 57.

2 Zhang J, Lu L, Cui G, Shen X, Yi H & Zhang W, *Mater Design*, 31 (2010) 2654.

3 Manfridini A P de A, Durãesde Godoy G C & Santos L de A, *J Mater Res Technol*, 6 (2017) 65.

4 Nikolova M, Nikolov D, Derin B & Yankov E, *MATEC Web of Conferences, 4th International Conference on Computing and Solutions in Manufacturing Engineering - CoSME'16*, 94 (2017), ISSN 2261-236X.

5 Nikolova M, Danev P & Dermendzhiev I, *Mater Sci Technol*, 21 (2013) 84.

6 King P C, Reynoldson R W, Brownrigg A & Long J M, *Surf Eng*, 21 (2005) 99.

7 Zheng J, Zhang S H, Wu P, Kwon S C, Li M X, Liu S Y & Chen W L, *Ceramics Int*, 41 (2015) 2519.

8 Akbari A, Mohammad Zadeh R, Templier C & Riviere JP, *Surf Coat Tech*, 204 (2010) 4114.

9 Kula P, Wolowiec E, Pietrasik, Dybowski K & Januszewicz B, *Vacuum*, 88 (2013) 1.

10 Hernandez M, Staia M H & Puchi-Cabrera ES, *Surf Coat Tech*, 202 (2008) 1935.

11 Danev P, *Eng Sci*, 41 (2004) 73.

12 Hasan M M, Haseeb A S M A & Masjuki H H, *Surf Eng*, 28 (2012) 778.

13 Akono A-T, Reis P & Ulm F-J, *Phy Rev Let*, 106 (2011) 20.

14 Bale CW, Bélisle E, Chartrand P, Decterov S A, Eriksson G, Gheribi AE, Hack K, Jung I-H, Kang Y-B, Melançon J, Pelton A D, Petersen S, Robelin C, Sangster J, Spencer P & VanEnde M-A, *Calphad*, 55 (2016) 1.

15 Zhu B & Kelly G L, *Mater Forum*, 27 (2004) 54.

16 Zhang L, Ren C, Yu Q, Zhang J, Sun S, Ren Q, Lian Y, Chen X & Gao W, *Surf Coat Tech*, 315 (2017) 95.

17 Nayebpashaee N, Soltanieh M & Kheirandish S, *Mater Manuf Process, 31* (2016) 1192.

18 King P C, Reynoldson R W, Brownrigg A & Long J M, *Surf Eng*, 21 (2005) 86.

19 Januszewicz B, Wolowiec E & Kula P, *Met Sci Heat Treat*, 57 (2015) 32.

20 Psyllaki P, Kefalonikas G, Pantazopoulos G, Antoniou S & Sideris J, *Surf Coat Tech*, 162 (2002) 67.

21 Sohi M H, Ebrahimi M, Raouf A H & Mahboubi F, *Surf Coat Tech*, 205 (2010) S84.

22 Rocha A da S, Strohaecker T, Tomala V & Hirsch T, *Surf Coat Tech*, 115 (1999) 24.

23 Ueda M, Leandro C, Reuther H & Lepienski C M, *Nucl Instrum Methods Phys Res B*, 240 (2005) 204.

24 Hong J M, Cho U Y R, Kim D J, Baek J M & Lee K H, *Surf Coat Tech*, 131 (2000) 548.

25 Zlatanovic M, Popovic N, Bogdanov Z & Zlatanovic S, *Surf Coat Tech*, 174 (2003) 1220.

26 Zlatanovic M, Popovic N, Bogdanov Z & Zlatanovic S, *Surf Coat Tech*, 177 (2004) 277.

27 Cavaliere P, Zavarise G & Perillo M, *Comput Mater Sci*, 46 (2009) 26.

28 Shu-Hung Y, Liu-Ho C & Heng C, *Engineering*, 3 (2011) 42.

29 Fares M L, Belaid M, Chahaoui O & Ghous H, *e-J Surf Sci Nanotech*, 10 (2012) 1.

30 Wen D-C, *Wear*, 268 (2010) 629.